Large Area Metal Nanowire Arrays with Tunable Sub-20 nm Nanogaps

Loan Le Thi Ngoc,[§,†] Mingliang Jin,[§,†,‡] Justyna Wiedemair,[†] Albert van den Berg,[†] and Edwin T. Carlen[†,*]

[†]BIOS Lab on a Chip Group and MESA+ Institute for Nanotechnology, University of Twente, Enschede, The Netherlands and [‡]Institute of Electronic Paper Display, South China Academy of Advanced Optoelectronics, South China Normal University, Guangzhou, China. [§]L.L.T.N. and M.J. contributed equally to this work

ABSTRACT We report a new top-down nanofabrication technology to realize large area metal nanowire (m-NW) arrays with tunable sub-20 nm separation nanogaps without the use of chemical etching or milling of the metal layer. The m-NW array nanofabrication technology is based on a self-regulating metal deposition process that is facilitated by closely spaced and isolated heterogeneous template surfaces that confine the metal deposition into two dimensions, and therefore, electrically isolated parallel arrays of m-NW can be realized with uniform and controllable nanogaps. Au-NW and Ag-NW arrays are presented with high-density $\sim 10^5$ NWs cm^{-1}, variable NW diameters down to $\sim$50 nm, variable nanogaps down to $\sim$5 nm, and very large nanogap length density $\sim$1 km cm^{-2}. The m-NW arrays are designed and implemented as interdigitated nanoelectrodes for electrochemical applications and as plasmonic substrates where the coupled-mode localized surface plasmon resonance (LSPR) wavelength in the nanogaps between adjacent m-NW dimers can be precisely tuned to match any excitation source in the range from 500 to 1000 nm, thus providing optimal local electromagnetic field enhancement. A spatially averaged (n = 2500) surface-enhanced Raman scattering (SERS) analytical enhancement factor of $(1.2 \pm 0.1) \times 10^7$ is demonstrated from a benzenethiol monolayer chemisorbed on a Au-NW array substrate with LSPR wavelength matched to a He–Ne laser source.

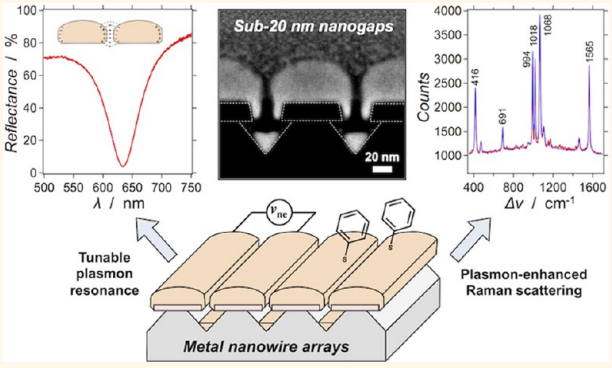

KEYWORDS: metal nanowire arrays · top-down nanofabrication · nanoelectrodes · metal nanograting · plasmonic substrates

Over the past decade, there has been increasing interest in metal nanowires (m-NW) due to their unique electronic, optical, and electrochemical properties.[1] There are different types of m-NW devices and substrates depending on the manufacturing method, such as one-dimensional quantum confinement devices,[2] vertical m-NW arrays,[3] and aligned planar m-NW arrays.[4] A full review of previous work on m-NW is beyond the scope of this article, and we refer to a recent review that highlights many of the different m-NW types and fabrication techniques.[5] In this article, we are interested in aligned planar m-NW arrays, commonly referred to as nanogratings, with pitch dimensions of $\sim$100 nm and nanogap dimensions between adjacent m-NWs <20 nm, which are especially important for both electrical nanogap biochemical sensors[6] and the emerging field of plasmonics,[7] where controllable and uniform nanogap dimensions over large areas are typically required.

There are many techniques available to fabricate planar NW arrays that can be broadly classified as either bottom-up or top-down. Bottom-up nanofabrication is, in principle, simple and provides many high quality materials; however, suitable methods for accurate nanowire alignment are lacking, thus making this approach problematic for manufacturing large area m-NW arrays, and will be described in more detail in the plasmonic substrate section. Top-down nanofabrication techniques currently provide the best approach to manufacture arrays of aligned m-NW with sub-20 nm separation nanogap dimensions. Conventional top-down nanopatterning techniques, such as deep-ultraviolet and immersion deep-ultraviolet stepper photolithography, are currently the standard for semiconductor manufacturing; however, these techniques are expensive and accessible only to large integrated circuit manufacturers. Serial nanopatterning techniques, such as electron beam lithography and focused ion

* Address correspondence to e.t.carlen@utwente.nl.

Received for review February 25, 2013 and accepted May 6, 2013.

Published online May 06, 2013
10.1021/nn4009559

beam milling can realize feature sizes below 10 nm; however, uniform chemical etching of polycrystalline gold and silver thin films over large areas can be problematic due to etch rate nonuniformity caused by grain size variations and poor photoresist adhesion, which manifests as rough nanostructure edges. In the case of ion beam milling metal materials, metal redeposition can be a limiting factor in machining nanoscale dimensions.[8]

In this article, we present a new m-NW fabrication technology that is based on a combination of conventional and well-characterized top-down microfabrication and nanofabrication steps to realize a template surface that facilitates the growth of the physical vapor deposited metal layer on the template surface, reduces the metal growth rate in the lateral direction between adjacent template surfaces, and allows for precise control of the separation nanogaps between adjacent NWs that are electrically isolated. The advantage of this new technology is that extremely dense arrays of electrically isolated metal-NWs that have controllable elliptical surface shapes and sub-20 nm separation nanogaps can be realized without the use of a metal etching or milling step. Furthermore, the m-NW arrays presented in this article can be reused by replacing the metal layer, which does not damage the template substrate materials or alter the template dimensions.

The m-NW arrays produced with the fabrication technology presented here are quite different than conventional subwavelength metal gratings[9,10] where the grating is formed by coating a nanostructured surface with a continuous metal thin film, and therefore, electrically isolated nanostructures separated by nanogaps are not possible, which precludes applications requiring electrically isolated nanoelectrodes. More recently, a metal nanograting was reported[11] that consists of isolated nanostructures that are separated by nanogaps, but however, requires an oblique substrate orientation with the metal deposition source to control the nanogap spacing, and also has not been shown as electrically isolated nanoelectrodes. We have fabricated both Au-NW and Ag-NW arrays and have conducted extensive characterization of the NW dimensions and cross-sectional shape using high-resolution scanning electron microscopy (SEM) and atomic force microscopy (AFM). A simple model has been developed that can be used as a design tool to estimate the nanogap dimensions based on the metal deposition process and template dimensions. Reflection spectroscopy is used to demonstrate the tunability of the nanogap dimensions and the uniformity of the array dimensions over large areas. The m-NW array substrates are implemented as interdigitated nanoelectrode substrates for electrochemistry applications and as plasmonic substrates for surface-enhanced Raman scattering (SERS).

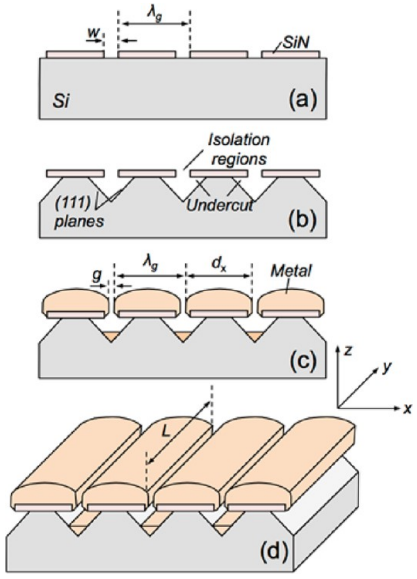

Figure 1. Top-down metal-NW array fabrication procedure and relevant dimensions (not to scale). (a) Lithographically patterned and etched SiN template layer with the length of the template aligned to the [110] direction of the (100) silicon wafer; (b) anisotropic etching of silicon to create the undercut regions; (c) metal deposition using conventional physical vapor deposition; (d) metal-NW array.

RESULTS AND DISCUSSION

The new metal-NW array nanofabrication technology is based on a self-regulating metal deposition process that is facilitated by closely spaced isolated heterogeneous template surfaces realized with a nanopatterned silicon nitride (SiN) layer formed on a structured silicon substrate, which is shown in the brief process sequence of Figure 1. The SiN template layer is first patterned with electron-beam lithography, where the length of the template is aligned parallel to the [110] direction of a conventional (100) silicon wafer, and selectively removed with reactive ion etching (Figure 1a). The SiN layer also serves as a hard mask for the anisotropic plane-dependent silicon wet etching step, which results in the well-controlled triangular undercut region in the silicon layer, where the (100) planes etch approximately 10 times faster than the (111) planes in an alkaline etchant (Figure 1b).

The resulting structure is a template surface that facilitates the growth of individual metal-NWs along the length of the SiN template (*y*-direction) while restricting the lateral (*x*-direction) growth of the metal due to the isolation regions of width *w*. A conventional physical vapor deposition method, that is, sputtering or evaporation, is used to deposit the polycrystalline metal layers. The undercut sections prevent the metal from forming a continuous layer, thus the individual NWs are similar to ultralong cylindrical nanoparticles. The edge of the etched SiN template layer induces internal stress in the growing metal layer, which results in the elliptically shaped upper surface of each NW in

the array (Figure 1c). The elliptical shape of the NWs, that is, the major and minor radii, is controlled by the metal layer thickness t_z and template pitch λ_g and will be described in more detail in the next section. This simple fabrication method can provide very uniform and high-density ($\sim 10^5$ NWs cm^{-1}) metal-NW arrays with small NW diameters (lower limit, $d_x \approx 50$ nm), small NW separation nanogaps (lower limit, $g \approx 5$ nm), large length to pitch ratio ($L/\lambda_g > 10^4$), and extremely large nanogap length density (~ 1 km cm^{-2}) (Figure 1d) without the use of etching or milling the metal layer.

Figure 2 shows high-resolution SEM images that are representative of Au-NW arrays fabricated with the technology reported in this article. The SEM images clearly demonstrate the effectiveness of this fabrication technology for manufacturing high quality uniform metal-NW arrays with well-controlled sub-20 nm separation nanogaps using conventional microfabrication and nanofabrication techniques (Figure 2a). Figure 2b shows an SEM image of an Au-NW array cross-section, prepared with focused ion-beam milling, which demonstrates that electrically isolated Au-NWs with uniform shape and sub-20 nm separation nanogap can be realized. Although electron-beam lithography has been used to pattern the template surface isolation region gap, any conventional high-throughput photolithography method, such as deep ultraviolet-stepper lithography or laser interference lithography,[10−12] can be used to pattern the template surfaces over entire wafer areas. Ag-NW arrays have also been realized with this fabrication technique and have similar characteristics as the Au-NW arrays (Figure S1, Supporting Information). The small triangular metal deposited at the base of the isolation pit results from the deposition method, and is physically disconnected from the adjacent NWs located on the template surface.

Figure 3 shows representative SEM cross sections and high-resolution AFM three-dimensional topography images of an Au-NW array with $\lambda_g = 150$ nm (Figure 3c) and $\lambda_g = 100$ nm (Figure 3d). The NW shape and separation nanogap are remarkably uniform considering that a conventional physical vapor deposition method is used. The separation nanogap in this case is $g \approx 10$ nm and is quite well controlled. Figure 3b shows experimental measurements of nanogap width g for different surface template separation widths w, and nominal metal thickness t_z. The nanogap width decreases rapidly during the initial deposition of $\sim$20 nm and then reduces as g becomes smaller. The measured nanogap widths g can be estimated with an empirical relationship $g = w\,e^{-\alpha t_z}$, where $\alpha \approx 0.02$ nm^{-1} is the nanogap reduction parameter, which has been determined by fitting to the measured template width w and nominal metal thickness t_z shown in Figure 3b (Figure S2, Supporting Information). Figure 3c clearly illustrates that the metal-NWs with sub-20 nm nanogaps are physically isolated. From the structure dimensions

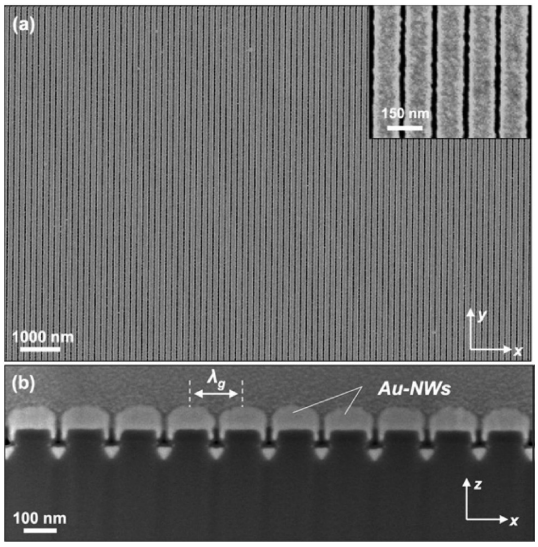

Figure 2. High-resolution SEM (acceleration voltage, 2 kV) images of fabricated Au-NW arrays. (a) Large area (15 × 15 μm^2) NW array with λ_g = 150 nm pitch and g = 20 nm nanogap spacing (magnification, 45 k×); (b) Au-NW array cross-section with λ_g = 150 nm and $g \approx$ 10 nm (magnification, 305 k×).

shown in Figure 3a, the lateral metal overlap thickness of the deposited metal layer can be estimated with $2t_x = w(1 - e^{-\alpha t_z})$, which can be used to design the separation nanogaps between adjacent NWs in the array. The NW surface follows an elliptical shape with major radius e_x and minor radius e_z, as shown in Figure 3c. The major radius can be estimated with $2e_x \approx \lambda_g - w\,e^{-\alpha t_z}$, and the minor radius estimated with $2e_z = t_z + t_{SiN}$, where t_{SiN} is the thickness of the SiN layer, λ_g and w are defined by the template patterning method (Figure 1a), and t_z is the nominal metal thickness, all of which can be well-controlled. Interestingly, as λ_g is reduced in this case, the NW cross-section approaches a circular shape that is, $e_z \approx e_x$ (Figure S3 and Figure S4, Supporting Information), which allows for an elliptical cross-section with tunable major and minor axis dimensions. From Figure 3c, the measured minor radius $e_z \approx 50$ nm corresponds very well to $(t_z + t_{SiN})/2$, where $t_z = 70$ nm and $t_{SiN} = 30$ nm, which were determined with separate AFM measurements. For $\lambda_g = 150$ nm, $w = 50$ nm, $t_z = 70$ nm, and $\alpha = 0.016$ nm^{-1}, $e_x \approx 67$ nm, which corresponds well to the measured major radius of 65 nm (Figure 3c).

Figure 4 shows SEM images of Au-NW arrays with different pitches ranging from $\lambda_g = 100$ nm (Figure 4a) to $\lambda_g = 250$ nm (Figure 4d) and different nanogap widths ranging from g = 20 nm (Figure 4a) to g = 10 nm (Figure 4d). Since the NW dimensions and separation nanogaps can be well-controlled, the fabrication technology provides isolated metal nanostructures that have similar shape and dimensions of conventional metal cylindrical nanoparticles; however, the top-down fabrication approach, that results in high-density

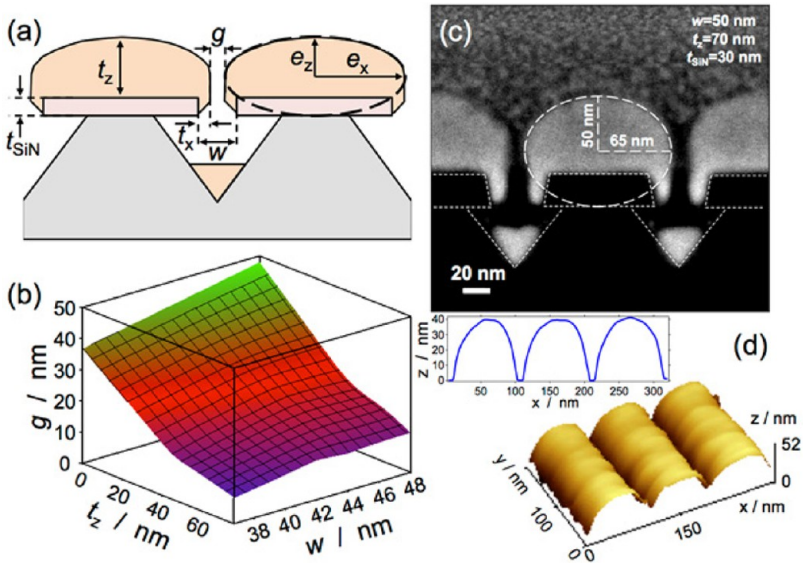

Figure 3. Au-NW array nanogap and surface shape. (a) NW array cross-section schematic with characteristic dimensions. Black dashed line shows the ellipse major radius e_x and minor radius e_z; (b) Measured nanogap width g as a function of the nominal Au thickness t_z and the template isolation width w; (c) High-resolution SEM image of Au-NW array cross-section prepared with focused ion beam milling with λ_g = 150 nm and $g \approx$ 10 nm (acceleration voltage, 2 kV; magnification, 300 k×). White dotted lines indicate template cross-section profile (*i.e.,* SiN and silicon layers). White dashed lines indicate the elliptical surface profile with e_z = 50 nm and e_x = 65 nm; (d) High-resolution three-dimensional AFM image of upper surface and corresponding two-dimensional profile (inset) of Au-NW array with λ_g = 100 nm and $g \approx$ 10 nm.

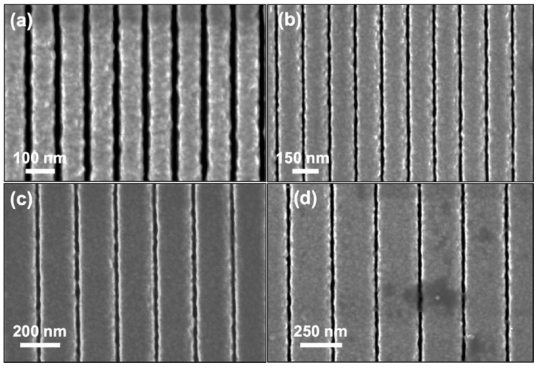

Figure 4. High-resolution SEM images of fabricated Au-NW arrays with tunable pitch λ_g and nanogap with g (acceleration voltage, 2 kV; magnification, 300 k×). (a) λ_g = 100 nm, g = 20 nm; (b) λ_g = 150 nm, g = 10 nm; (c) λ_g = 200 nm, g = 10 nm; (d) λ_g = 250 nm, g = 10 nm.

well-aligned NW arrays that are self-forming with sub-20 nm nanogaps, does not provide isolated nanostructures without the use of metal etching or milling, which is problematic for most polycrystalline noble metals due to nonuniform material etching, as previously described. Many applications, such as biosensing,[6] electrochemistry,[13] and plasmonics[14] can benefit from the large area metal-NW arrays reported in this article.

Nanoelectrode Substrate. The metal-NW arrays can be patterned into functional interdigitated (ID) nanoelectrode arrays with the number of nanogaps ranging from one up to thousands. Figure 5a shows a schematic of a 4-nanogap ID nanoelectrode array and Figure 5b shows an SEM image of fabricated 49-nanogap ID nanoelectrode array device with λ_g = 200 nm and g = 20 nm. The application of voltage v_{ne} provides a controllable electric field across each of the nanogaps. This configuration can be used for a variety of applications, such as the study of molecular conductance[15] from molecules that bridge the nanogap width, electrochemical nanosensors,[13] and combined electrochemical and surface spectroscopy.[16]

The electrical behavior of the Au-NWs, and the electrical isolation of Au-NW pairs separated by a nanogap, is evaluated using the test structure shown in the inset of Figure 5c, which shows two Au-NWs of width w_{nw} and length L_{nw}, separated by a nanogap width g_{nw}. The DC electrical resistance R_{1-2} (and R_{3-4}) of the test structures is measured for three different device lengths L_{nw} (20, 40, and 60 μm), and subsequently fit to $R_{nw} = \rho_{p\text{-}Au}L_{nw}/A_c$, where $\rho_{p\text{-}Au}$ is the resistivity of the polycrystalline Au layer with thickness and A_c is the cross-sectional area of a single NW structure. The average DC resistance measurement of three Au-NWs at each device length is shown Figure 5c (open circles). The solid line in Figure 5c shows the fit to the measured data with $\rho_{p\text{-}Au} = (6.24 \pm 0.67) \times 10^{-6}$ Ω-cm, which is larger than the electrical resistivity of bulk polycrystalline Au samples,[17] and consistent with resistivity measurements of thin polycrystalline Au layers where the electrical resistivity is shown to be inversely proportional to the electronic mean free path (mfp), and increases significantly when the film thickness is less than the mfp.[18] The Au-NW electrical isolation has been measured from over 20 device structures and $R_{1-4}(R_{2-3}) > 100$ MΩ (measurement limit of the digital

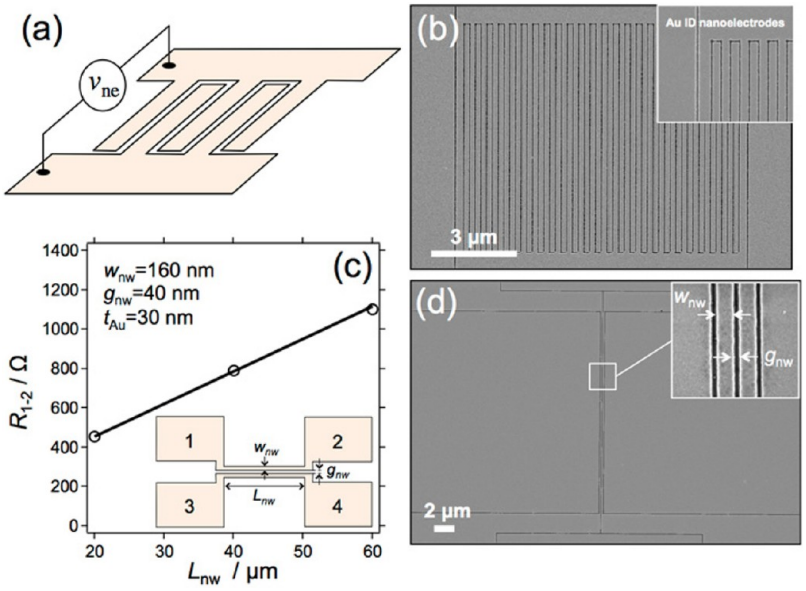

Figure 5. Interdigitated metal nanoelectrode substrate. (a) 4-Nanogap ID nanoelectrode configuration; (b) SEM image of 49-nanogap Au ID nanoelectrode device with λ_g = 200 nm and g = 20 nm (acceleration voltage, 2 kV; magnification, 14 k×); (c) measured (open circles) Au-NW resistances R_{1-2} from test structure shown in inset with as a function of device length L_{nw} (20, 40, and 60 μm). The fit to the data is shown as a solid line. Each measured data point represents the average of three measurements from different device structures; (d) SEM image of representative Au-NW test structure with L_{nw} = 20 μm.

multimeter instrument) for the device and layer dimensions tested.

Plasmonic Substrate. The metal-NW arrays are well suited for plasmonics applications, which use metal nanostructures that couple far-field electromagnetic radiation into electromagnetic surface modes, called surface plasmon polaritons (SPP), that are confined to the interface of a nonabsorbing dielectric, with positive real dielectric constant, to a conductive material with negative real value of its dielectric function, which is typically a noble metal. The generation of the surface plasmon modes on metal surfaces has been studied extensively ranging from one-dimensional SPP mode confinement on flat surfaces to localized surface plasmon resonance (LSPR) mode confinement in two dimensions on cylindrical nanostructures and three-dimensional mode confinement on spherical nanostructures; in all cases the confined surface plasmon modes result in an enhanced electromagnetic field magnitude at the surface interface $M_s(\vec{r},\omega) = |\vec{E}_s(\vec{r},\omega)|/|\vec{E}_o(\vec{r},\omega)|$, where $\vec{E}_s(\vec{r},\omega) \equiv \vec{E}_s(x,z,\omega)$ is the total local electromagnetic field at the metal surface and $\vec{r}$ is a position vector. More importantly, when two metal nanoparticles are in close proximity with $g < d_x$ (Figure 6), the enhanced electromagnetic fields around each nanostructure coherently interfere, thus resulting in a coupled-plasmon electromagnetic field $\vec{E}_c(\vec{r},\omega)$ across the nanogap, which results in an increased in the electromagnetic field enhancement $M_c(\vec{r},\omega) = |\vec{E}_c(\vec{r},\omega)|/|\vec{E}_o(\vec{r},\omega)|$, when the excitation polarization is aligned along the interparticle axis (Figure 6). For small nanogaps, where g < 20 nm, the coupled-plasmon enhancement increases rapidly and typically results in $M_c \gg M_s$.[14,19]

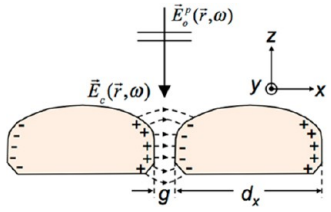

Figure 6. Plane (p-polarized) wave excitation $\vec{E}_o^p(\vec{r},\omega)$ of coupled local surface plasmon resonance between a closely spaced metal-NW and resulting coupled electromagnetic field $\vec{E}_c(\vec{r},\omega)$.

The coupled-mode plasmon resonators have important applications in surface spectroscopy,[20] fluorescence enhancement,[21] energy conversion,[22] and nanoscale optics.[23]

Currently, the major challenge in fully exploiting coupled-mode plasmon resonances on metals is the reproducible realization of large area metal nanostructure arrays with uniform sub-20 nm separation nanogaps in high density, as previously described. There have been many different types of plasmonic substrates that can be broadly categorized as isolated metal nanostructure arrays (IMN) and metal nanostructure arrays formed from a continuous metal layer (CMN). The IMN are typically realized with bottom-up fabrication techniques and come in many forms, such as colloidal nanoparticle suspensions[24−27] and self-assembled colloidal films.[28] Colloidal nanoparticle suspensions and films, which are relatively simple to prepare, however, typically have poor enhancement uniformity and reproducibility due to their random orientation and composition, lack of precise dimension control, separation spacing, and excitation polarization

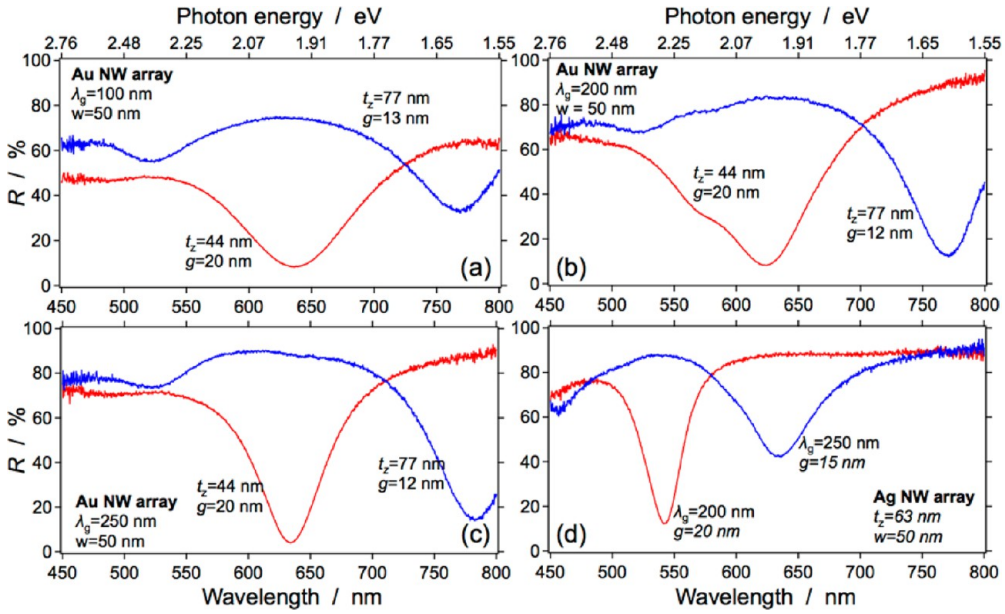

Figure 7. Measured reflectance of Au-NW and Ag-NW array surfaces with different pitch λ_g and nanogap width g showing the LSPR tuned to commonly used laser wavelengths (λ_L = 532, 633, and 785 nm). (a) Au-NW with λ_g = 100 nm and w = 50 nm; (b) Au-NW with λ_g = 200 nm and w = 50 nm; (c) Au-NW with λ_g = 250 nm and w = 50 nm; (d) Ag-NW with λ_g = 200 nm and g = 20 nm; and λ_g = 250 nm and g = 15 nm with template width w = 50 nm.

alignment, which is especially important for coupled-mode plasmon resonances. Top-down fabrication techniques have also been employed for the realization of IMN, such as nanosphere lithography,[29] electron-beam patterning, focused ion-beam milling, and nanoimprinting;[30−35] however, the formation of well-controlled nanogaps over large areas in high density remains problematic. CMN plasmonic substrates are usually realized with top-down fabrication techniques, such as electrochemically roughened surfaces[36] and surface templates coated with the active plasmonic layer,[37−40] which has not achieved surfaces with both high nanogap density and large enhancements over large areas.

The new nanofabrication technology described in this article combines the benefits of top-down fabrication technology, such as precise nanostructure alignment and metal thickness control, and the benefits of metal nanoparticle geometry, such as isolated nanostructures with two-dimensional field confinement and well-understood coupled-mode plasmon resonances. Metal grating structures have been reported for over three decades and typically consist of a continuous metal layer that is periodically roughened to facilitate the generation of SPP excitation such that the momentum of photons in the top dielectric layer is increased by the in-plane periodicity to phase-match to the surface plasmon.[41−48] Early research on the optical properties of metallic gratings typically reported grating pitches near the excitation wavelength[41−45] and later experimental and theoretical reports developed the basic understanding of the geometry-dependent optical properties of zeromode subwavelength nanogratings;[46−48] in all subwavelength nanograting structures, large electromagnetic field enhancements due to coupled-mode plasmon resonances are present in the nanogap region between adjacent nanostructures (Figure 6).

Reflection spectroscopy is used to demonstrate the plasmonic functionality, and tunability and uniformity of the dimensions of the metal-NW arrays, pitch λ_g and nanogap g, with a normally incident linearly polarized white light source that is aligned perpendicular to the nanogaps. Figure 7 shows examples of reflectance measurements of Au-NW and Ag-NW arrays where the reflectance decreases to a minimum value at a certain wavelength that corresponds to the LSPR coupling wavelength λ_L. For all measurements a flat Au, or Ag, surface is used as a reflectance reference. Figure 7 panels a, b, and c show that the LSPR wavelength (reflectance minimum) of Au-NW arrays with different λ_g and g (realized using different Au thickness t_z) can be precisely tuned to 633 and 785 nm, commonly used laser wavelengths used in visible spectrum plasmonics applications. The Au-NW array with λ_g = 200 nm and g = 20 nm (Figure 7b) shows two resonances, and the origin of the higher energy resonance is not known and further investigation is required. Figure 7d shows that the LSPR wavelength can be tuned to 532 and 633 nm for a fixed Ag thickness t_z nm and different λ_g and g. In all cases, λ_L red-shifts when g is decreased, hence demonstrating a strong dependence on the couple-resonance mode in the nanogap.

The LSPR can be assessed with the resonance quality factor Q, which is a dimensionless metric that

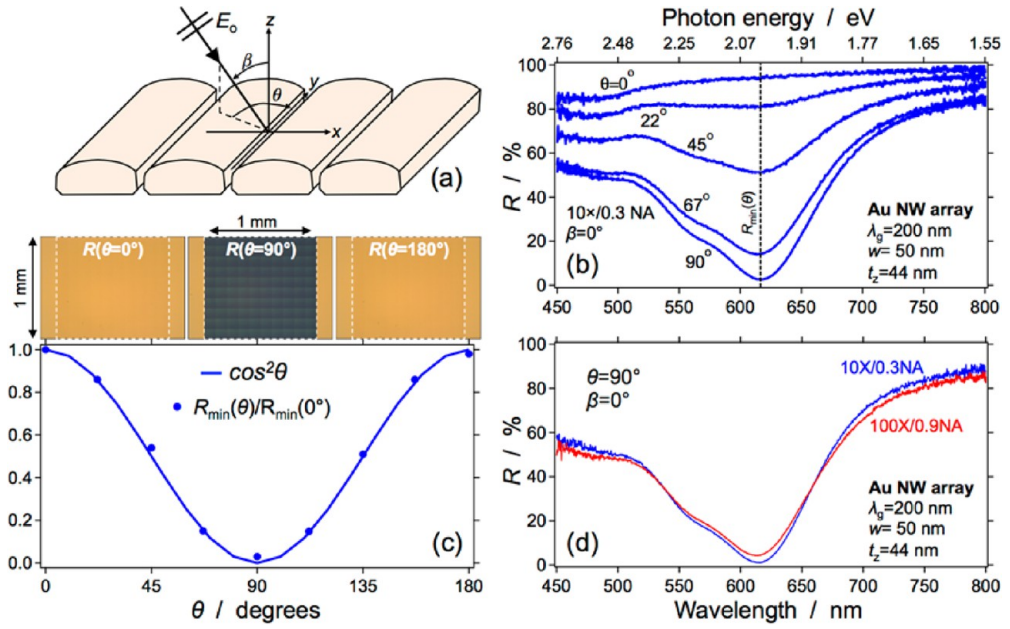

Figure 8. Measured local surface plasmon resonance dependence on the excitation polarization alignment to nanogap. (a) Reflectance measurement configuration; (b) reflectance as the azimuthal angle of the p-polarized excitation source is varied from $\theta = 0°$ (no coupling) to $\theta = 90°$ (coupled); (c) measured normalized reflectance minimum $R_{min}(\theta)/R_{min}(0°)$ (solid dots) and $\cos^2(\theta)$ (solid line) demonstrating the plasmonic coupling dependence. Upper inset: reflectance images of Au-NW surface (outlined in white dashed line) for different polarization alignments $\theta = 0°$ (no coupling), $\theta = 90°$ (coupled with dark blue reflected color), and $\theta = 180°$ (no coupling); (d) measured reflectance of Au-NW array with high magnification objective (100 × /0.9 NA) and low magnification objective (10 × /0.3 NA).

represents the ratio of energy stored in the resonator to energy loss per cycle. The experimental quality factor can be estimated with $Q_L \approx \lambda_L/\Delta\lambda$, where $\Delta\lambda$ is the full-width half-maximum of the reflectance LSPR and λ_L is the wavelength at the minimum reflectance R_{min}. The LSPR mode shape was modeled with a Lorentzian function and the corresponding $\Delta\lambda$ determined. The quality factor of the Au-NW array with λ_g =250 nm and g = 20 nm is $Q_L \approx 10$ (Figure 7c), and for the Ag-NW array with λ_g = 200 nm and g = 20 nm $Q_L \approx 15$ (Figure 7d). The relatively low experimental quality factors are typical for noble metals, such as Au and Ag, due to absorptive damping in the metal;[50,51] however, some inhomogeneous broadening of the resonance dip occurs to the finite surface roughness of the polycrystalline metal layer.

The LSPR coupling is dependent on the alignment of the polarization of the normally incident ($\beta = 0°$) excitation source to the Au-NW nanogap as shown in reflectance measurements in Figure 8. The polarization of the white light excitation is fixed and the sample is rotated from $\theta = 0°$, where the source excitation polarization is parallel to the length of the NW (s-polarized) to $\theta = 90°$, where the electric field polarization of the source excitation is perpendicular to the length of the NW array (p-polarized) (Figure 8a). The LSPR coupling dependence on the excitation polarization is clearly shown as the magnitude of the reflectance dip decreases as excitation is rotated from p-polarization to s-polarization where no plasmonic coupling occurs and the reflectance of the subwavelength surface is similar to a flat (as-deposited) Au surface.

As is well-known from electromagnetic theory, the total electric field outside of the metal-NW is $\vec{E}_s = \vec{E}_o + \vec{E}_i$, where $\vec{E}_o$ is the incident electric field and $\vec{E}_i$ is the induced or scattered electric field.[51,52] Similar to the scattering theory of metal nanoparticles, $|\vec{E}_s|^2 = I_s^{\perp} \sin^2\theta$, where $I_s^{\perp}$ is the total intensity perpendicular to the plane of incidence, which is dependent on the excitation polarization alignment to the nanostructure, and therefore, the reflectance of the metal-NW arrays is modulated according to the alignment of the excitation polarization to the nanogaps as a function of azimuthal angle θ (Figure 8a). The polarization-dependent reflectance from an Au-NW array surface (Figure 8b) shows that the p-polarized excitation aligned perpendicular to the nanogap ($\theta = 90°$) results in the strongest plasmonic coupling of the incident radiation in the nanogap and subsequent reflectance dip R_{min} at the coupling wavelength λ_L, which corresponds to the maximum $|\vec{E}_s|^2$ and $|\vec{E}_c|^2$. As the alignment angle is rotated to $\theta = 0°$, where the p-polarized incident radiation is aligned parallel to the nanogap, no plasmonic coupling in the nanogap occurs, that is, minimum $|\vec{E}_s|^2$, and the subwavelength pitch Au-NW surface exhibits a reflectance similar to the flat Au surface. Consequently, the minimum reflectance is dependent on the alignment angle according to $R_{min}(\theta) \propto \cos^2(\theta)$, as shown in Figure 8c. The inset images of the reflectance images of a large area

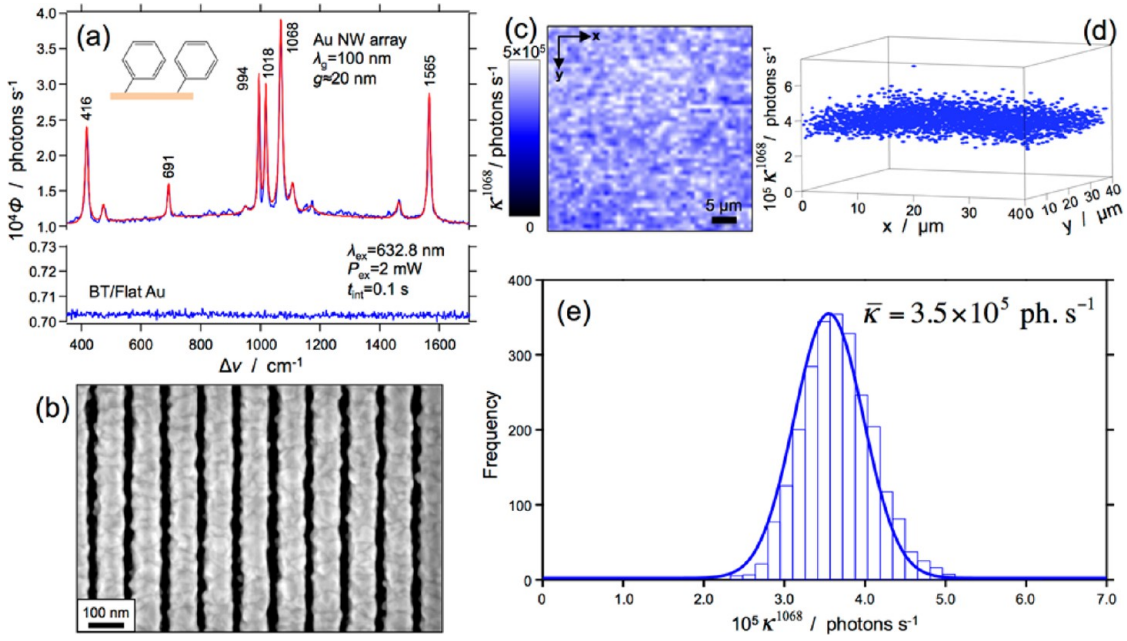

Figure 9. Measured SERS spectra of BT chemisorbed on Au-NW array and flat-Au surfaces. (a) Top: measured (red) spectrum from surface with pitch λ_g = 100 nm and g = 20 nm (measured with SEM), and modeled Lorentzian bands (blue). Bottom: measured spectrum from BT chemisorbed on a flat (as-deposited) Au layer. (b) SEM image of Au-NW array surface (acceleration voltage, 2 kV; magnification, 300 k×); (c) Raman image of the integrated intensity of the 1068 cm^{-1} band over a 40 × 40 μm^2 area; (d) three-dimensional scatter plot of the 1068 cm^{-1} band integrated intensity; (e) histogram of 1068 cm^{-1} band integrated intensity from Raman image and modeled Gaussian distribution.

(1 mm^2) Au-NW array show the plasmonic coupling of the p-polarized incident radiation is aligned parallel (θ = 0° and θ = 180°) to the length of the NWs, where no plasmonic coupling occurs and the reflected image color in the patterned region (within the white dashed lines) is similar to the unpatterned Au layer (outside the white dashed lines), and for the p-polarized incident radiation aligned perpendicular (θ = 90°), where the strong plasmonic coupling is evident by the reflected color change to dark blue in the patterned regions (Figure 8c). The dark blue reflected color corresponds to a yellow complementary color, which corresponds to a $\lambda_L \approx$ 633 nm from R_{min} (θ = 90°), as shown in Figure 8b.[53] The uniformity of the Au-NW array surface with λ_g = 200 nm and g = 20 nm is demonstrated using reflectance spectroscopy, as shown in Figure 8d, where the reflection spectrum collected using a low magnification microscope objective (10 × /0.3 NA) with a large spot diameter is shown with the reflection spectra collected with a high magnification microscope objective (100 × /0.9 NA) with a much smaller spot diameter. The large area reflectance spectra are nearly identical to the small area reflectance measurements, thus demonstrating the high degree of uniformity in the pitch and nanogap dimensions of the Au-NW arrays.

The Au-NW arrays are applied as SERS substrates by covering the Au-NW array surface with a monolayer of benzenethiol (BT) molecules, which provides an estimation of the uniformity of the spatially averaged enhancement factor from a small number of molecules. BT is a commonly used SERS probe molecule since it has a small number of well-characterized and strong Raman active modes, and does not fluoresce in the visible spectrum (Figure S5, Supporting Information). The measured Raman intensity (in units of photons s^{-1}) of a vibration band can be estimated with $\phi_i^v = (I_o/\hbar\omega_o)\sigma_v^R\sum_{j=1}^{N} G_{i,j}^{EM}G_{i,j}^{Ch}$, where i is the measurement location, j represents each molecule in the measurement collection volume, that is, objective spot size for a monolayer on a surface, v is the vibration band, I_o is the power on the excitation source with energy $\hbar\omega_o$, σ_v^R is the Raman scattering cross-section of band v, N is the total number of molecules in the collection volume, $G_{i,j}^{EM}$ is the electromagnetic enhancement factor, and $G_{i,j}^{Ch}$ is the chemical enhancement.[53] The electromagnetic enhancement can be estimated as $G_{i,j}^{EM}(\vec{r},\omega) \approx M_{c_{i,j}}(\vec{r},\omega_o)^2 \cdot M_{c_{i,j}}(\vec{r},\omega_o - \omega_v)^2$, where ω_o is the incident radiation frequency and the scattered radiation has vibrational frequency ω_v. It is commonly accepted that electromagnetic enhancement dominates the enhancement process, and therefore, $\phi_i^v \approx (I_o/\hbar\omega_o)\sigma_v^R G_i$, where $G_i \approx \langle G_i^{EM}\rangle$ is an ensemble average enhancement factor from the N molecules in the collection volume at each measurement location i, which is a similar effect reported for fluorescence spectroscopy,[54] and significantly affects the measured Raman intensities.

In Figure 9a, a representative SERS spectrum of a BT chemisorbed monolayer on a Au-NW array surface is shown with the dominant Raman active vibrational modes: 416, 691, 994, 1018, 1068, and 1565 cm^{-1}, all of which have been previously reported; the 416, 691, and

1068 cm^{-1} bands are due to a combination of the ring modes and C−S stretch mode, the 994 cm^{-1} band is due to a ring mode, the 1018 cm^{1} band from an H-stretch, and the 1565 cm^{-1} band represents a C−C ring stretch mode.[55] Note that the absence of the 917 cm^{-1} vibration mode, which is present in the normal Raman BT spectrum (Figure S6, Supporting Information), in the SERS spectrum is a good indicator of BT monolayer formation. The measured spectrum of BT on a flat Au layer is also shown in Figure 9a, which does not contain any detectable vibration bands and establishes the background noise floor of the measurement system. Also, note that the broad background signal is not present in the BT chemisorbed to the flat Au surface (Figure 9a) or the neat BT solution measurements (Figure S6, Supporting Information).

Each vibration band of a measured SERS spectrum at each measurement location is modeled with a Lorentzian function, and the background signal is modeled with a polynomial function. The integrated intensity of each vibration band κ_i^v was calculated by integrating the area of the fitted Lorentzian function after the removal of the background. The fitting accuracy of the Lorentzian function was comparable to the Voigt functions and is used for modeling all measured vibrational spectra. An example of a modeled spectrum is shown in the upper plot (blue solid line) of Figure 9a. Figure 9b shows a high resolution SEM image of the Au-NW array surface used for the measurements shown in Figure 9. The average nanogap spacing $g = 22 \pm 2$ nm, which was estimated from the 10 nanogaps (black regions) is shown in Figure 9b. Figure 9c shows a Raman image of the integrated intensity of the combined ring-bending and C−S stretch modes (1068 cm^{-1} band) from 2500 full spectra measured over an area of 1600 μm^2, which demonstrates the high spatial uniformity of the nanogap LSPR of the Au-NW array substrates, where 100% of the measured locations generate very large Raman intensities. The integrated intensity of the 1068 cm^{-1} vibration band is shown in the spatial Raman integrated intensity image map (Figure 9c) and the three-dimensional scatter-plot shown in Figure 9d. The histogram of the measured integrated intensity and fitted Gaussian distribution with mean $\bar{\kappa}^{1068} = 3.5 \times 10^5$ photon s^{-1} and standard deviation $s_\kappa^{1068} = 0.4 \times 10^5$ photon s^{-1} is shown in Figure 9e. From the scatter and histogram plots, the measured SERS spectra is highly uniform with every measurement location providing a large enhancement factor with about 11% variation across the measured surface, which we attribute to the new fabrication technique with controllable and uniform nanogaps with extremely large nanogap length density (~1 km cm^{-2}) that provides a large number of scattering hot-spots at each measurement location. Additionally, the sample-to-sample variation has been estimated at about 10%.

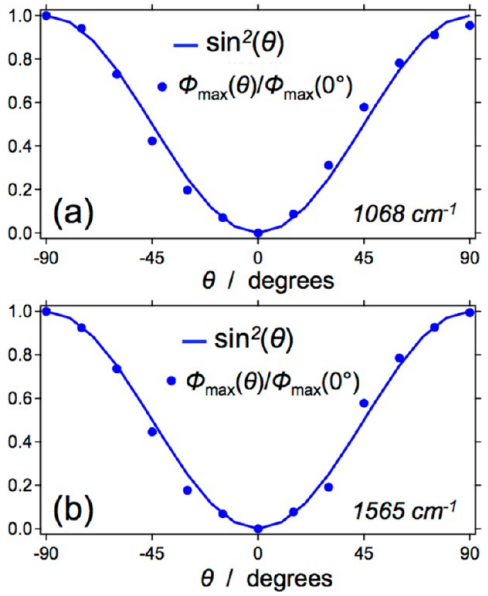

Figure 10. Normalized polarization-dependent Raman intensity measurements of chemisorbed BT on Au-NW array surfaces with pitch $\lambda_g = 200$ nm and $g = 20$ nm (measured): (a) 1068 cm^{-1} band; (b) 1565 cm^{-1} band.

The analytical enhancement factor is commonly used to assess the magnitude of the experimental Raman enhancement ${}^{AEF}G_i \approx (\kappa_i^v/N_{SERS})(\kappa_{NR}^v/N_{SR})^{-1}$, where κ_i^v and κ_{NR}^v are the integrated intensities from the SERS and conventional Raman measurements, respectively, and N_{SERS} and N_{NR} are the number of molecules in the collection volume of each measurement. Furthermore, the spatially averaged SERS enhancement of the 1068 cm^{-1} band estimated from 2500 spatial Raman data (Figure 9b,c), and conventional Raman measurements of neat BT, is ${}^{AEF}\bar{G} \approx 1.2 \times 10^7$, which is extremely large considering that all of the BT molecules chemisorbed to the Au-NW surface have been included in the estimation of the enhancement factor, while it is well-known that the molecules in the nanogap region generate the majority of the measured signal. The standard deviation of the spatially averaged SERS enhancement factor is 0.1×10^7, which represents an 11% enhancement factor variation averaged over the 2500 measurements. The large spatially averaged SERS enhancement and small variance demonstrated in the histogram shown in Figure 9e is very significant compared to previously reported distributions,[12] where a significant number of measurement locations on the surface were not enhanced as evidenced by a spatial intensity distribution shifted significantly toward zero, or low average enhancement factor. Similar SERS measurement results were obtained from Ag-NW arrays with chemisorbed BT monolayers and $\lambda_{L\text{-}Ag} \approx \lambda_o = 532$ nm (Figure S7, Supporting Information).

As previously described, the generation of the LPSR is dependent on the alignment of the excitation

polarization with the nanogaps, and since the magnitude of the electromagnetic field in the nanogap $|\vec{E}_c|$ is related to the SERS enhancement as $G_i \propto |\vec{M}_c|^4$, then optimizing the polarization alignment to the nanogap also maximizes the SERS signal. For most plasmonic substrates, aligning the excitation polarization with the geometry of the nanostructures is very important to maximize the electromagnetic enhancement. The polarization alignment was performed by manual rotation of the excitation laser beam using a $\lambda/2$ rotator plate. From the polarization dependent reflectance measurements (Figures 8b and 8c), the minimum reflectance was shown to follow $R_m(\theta) \propto \cos^2(\theta)$, hence, the Raman enhancement is $G_i \propto \cos^2(\theta)$, and therefore, $\phi_{max}(\theta) \propto \sin^2(\theta)$, where the maximum Raman enhancement occurs at $\theta = 90°$, as shown in Figure 10.

CONCLUSIONS

In summary, a new metal-NW fabrication technology has been presented that is based on a combination of conventional microfabrication and nanofabrication steps to realize a template surface that eliminates the growth rate of physical vapor deposited metal layers in the lateral direction between adjacent template surfaces and allows for precise control of the separation nanogaps between adjacent NWs that are electrically isolated. The advantage of this new technology is that extremely dense arrays of electrically isolated metal-NWs that have controllable elliptical surface shapes and sub-20 nm separation nanogaps can be realized without the use of a metal etching or milling step. Additionally, the template surface can be reused by selectively replacing the metal layer. We have demonstrated that the new fabrication technology using Au and Ag noble metals deposited with conventional physical vapor deposition have a high degree of uniformity and dimension control using far-field reflectance measurements of the nanograting structure. Finally, Au-NW arrays and Ag-NW arrays were fabricated, and with the use of high-resolution SEM imaging to determine the nanogap dimensions, the localized surface plasmon resonance in the nanogap was systematically tuned to common excitation laser wavelengths, 633 and 532 nm. The specifically designed Au-NW array substrates were used to measure the SERS spectra of benzenethiol chemisorbed resulting in a spatially averaged Raman analytical enhancement factor of $(1.2 \pm 0.1) \times 10^7$ from 2500 measurement locations. Our simple metal-NW arrays can be manufactured in any conventional microfabrication cleanroom using the established design rules.

METHODS

Metal Nanowire Fabrication. Conventional (100) silicon substrates have been used for all template fabrication. First, a thin (~30 nm) low stress silicon nitride (SiN) layer is deposited onto the silicon device layer by low-pressure chemical vapor deposition (pressure, 100 mTorr; 77.5 sccm H_2SiCl_2, 20 sccm NH_3; temperature, 850 °C; deposition rate, 4 nm min^{-1}; refractive index, 2.2). A 100 nm polymethyl methacrylate (PMMA, MicroChem Corp.) electron-sensitive photoresist was spin-coated on a silicon substrate and exposed to a 95 pA electron beam (acceleration voltage, 10 kV; aperture size, 20 μm) with the area dose in the range of 90−120 μAs cm^{-2} (Raith150-TWO). The electron-beam exposure along the length of the SiN template was aligned to the [110] direction of the (100) silicon wafers using the wafer flat as a reference. The total template surface array of 1 mm^2 is written in 100 × 100 μm^2 sections. The exposed regions were developed in a 1:3 methyl isobutyl ketone/isopropanol solution for 30 s, followed by immersion in isopropyl alcohol. The exposed SiN regions were removed using reactive ion etching (parallel plate reactor; pressure, 10 mTorr; RF (13.56 MHz) power, 60 W; electrode voltage, −500 V; electrode temperature, 10 °C; 25 sccm CHF_3, 5 sccm O_2; etch rate, 60 nm min^{-1}) followed by removal on the remaining PMMA and surface cleaning with oxygen plasma. Prior to silicon etching, the native oxide on the exposed silicon regions was removed by immersion in 1% hydrofluoric acid solution for 1 min and subsequently rinsed with deionized water. The silicon was etched in a 1% KOH solution at 55 °C with stirring for 45 s and rinsed with deionized water for 2 min. The different crystal planes etch anisotropically by hydroxide ions in an alkaline solution where (111) planes have the lowest etch rate and (100) and (110) planes both have higher etch rates. The surfaces were then cleaned in a 3:1 piranha solution (H_2SO_4:H_2O_2) for 15 min, rinsed with deionized water for 2 min, and dried with N_2. The polycrystalline metal layer (Au and Ag) was sputtered-coated (DC source) from a high-purity target in Ar plasma with a deposition rate of 0.6 nm s^{-1}.

SEM Sample Preparation and Imaging. The Au-NW cross-section samples were prepared by depositing a 100 nm thick Pt protection layer onto the upper surface. The sample slices were prepared (by NanoPhysics BV, Enschede, The Netherlands) in a dual-beam FIB (FEI Tecnai G2 F20 X-Twin FEG) and SEM imaging (LEO 1550, Zeiss) was performed at acceleration voltages ranging from 2 to 10 kV. The average nanogap dimensions were estimated by analyzing the SEM images with an image processing program (ImageJ 1.46r, National Institutes of Health). The area of the nanogap was estimated by fitting a closed polygon along all nanogap edges. The area of each nanogap is $A_{ng} = g \times L$, where g is spatial average nanogap width and L is the length of the NWs, which is a fixed dimension in the SEM image. The area of each of the 10 nanogaps in Figure 9b was measured, and g was calculated. The average and standard deviation of the calculated nanogap widths were then calculated as $g = 22 \pm 2$ nm.

AFM Imaging. A Digital Instruments Dimension 3100 was used for all AFM images. All AFM images were obtained in tapping mode with ultrasharp (average tip diameter ~2 nm) single crystal silicon tips (SSH-NCH-10, NanoandMore, GmbH).

Electrical Measurements. Electrical measurements (2-wire) were recorded in air on a probe station (PM8, Karl Süss), using flexible probe tips (model 407-A, Probing Solutions, Inc.) to minimize damage to the thin Au layers while probing. The probe tips are connected to a digital multimeter (model 2100, Keithley) with a maximum resistance measurement range limit of 100 MΩ.

Reflectance Measurements. Normal incidence reflection measurements were performed with a p-polarized (LPVISB100, Applied Laser Technology) white light source (100 W tungsten xenon lamp) focused on the Au- and Ag-NW surfaces with a microscope objective (10 × /0.3 NA, Leica and 100 × /0.9 NA, Olympus). The reflected beam is collected by the same objective and passed through a multimode fiber (QP450-1-XSR, Ocean Optics) to the spectrometer with an integrated detector (HR4000, Ocean Optics). All measurements were calibrated with

a flat (nonpatterned) as-deposited Au or Ag surface on the same template surface with the same nominal metal thickness on the NW surface. The polarization-dependent reflectance measurements were done by first aligning the sample and rotation stage concentric. The reflectance minimum was then determined by manually rotating the sample and monitoring the reflectance measured with the spectrometer. The sample was rotated 180° from the initial position in increments of 22° and the reflectance was recorded.

Raman Spectroscopy Instrumentation. A confocal Raman microscope system (alpha300R, WITec GmbH) was used for the Raman measurements, which consists of a TE-cooled charge coupled device (DU970P−BV, Andor Technology, Belfast, Northern Ireland) and UHTS300 spectrometer (f/4 300 mm FL; grating, 600 lines mm^{-1}). A He−Ne laser (λ_o = 632.8 nm) in a backscatter configuration was focused on the surface using a 100 × /NA 0.9 microscope objective. The elastically scattered laser excitation was removed with an edge filter. The polarization alignment was performed by manual rotation of the excitation laser beam using a $\lambda/2$ rotator plate.

Raman Measurements. Au-NW array surfaces were fabricated with Au thickness t_z = 40 nm and w = 50 nm, and the reflectance minimum was measured to confirm that $\lambda_L \approx 633$ nm. Benzenethiol (BT) monolayers were prepared by placing clean Au-coated NW array surfaces into a 4 mM BT-ethanol solution for 4 h. The substrate was gently rinsed with dehydrated ethanol and dried with pure N_2 gas. Raman spectra of chemisorbed BT on both flat Au and patterned Au-NW array surfaces have been measured in an ambient air environment with a 2 mW power (measured at the entrance of the microscope objective) He−Ne laser focused on the sample surface with 100 × /NA 0.9 microscope objective (Olympus MPlan FLN). The integration time for all Raman spectra is 100 ms. The measured signal is presented in CCD counts. Spatial imaging was performed over a 40 × 40 μm^2 area with 50 measurements per line and 50 lines for a total of 2500 measurements per scanned image.

Data Processing and Enhancement Factor Estimation. All measured Raman spectra of benzenethiol (BT) have been modeled with a Lorentzian mode shape, and the background has been modeled with a cubic polynomial function. The measured Raman intensity ϕ^{υ} of vibration band υ, presented in units of photons s^{-1}, is modeled by fitting the Lorentzian function $f(\upsilon) = A[(\upsilon - \upsilon_o)^2 + B]^{-1}$, where υ_o is the center vibration shift and A and B are constants, after removal of the background. The integrated intensity is calculated from the modeled vibration mode $\kappa = \int_{-\infty}^{+\infty} f(\upsilon)\, d\upsilon$ in units of photons s^{-1}. The spatially resolved SERS spectra (n = 2500) were modeled with Lorentzian functions and the background with a cubic polynomial function, and subsequently the integrated intensity κ_i^{υ} of each vibrational mode from i measurement locations was calculated. The number of chemisorbed BT molecules probed on the SERS surface is estimated as $N_{SERS} = A_s D_{BT} \approx 3.4 \times 10^6$ molecules, where A_s = 1.04×10^{-12} m^2 is the Au-NW surface area with λ_g = 100 nm, g = 20 nm and a half-ellipse cross-section (e_x = 40 nm and e_z = 40 nm) in a 1 μm diameter microscope objective spot size, which includes 10 Au-NWs and 10 nanogaps. $D_{BT} = 3.3 \times 10^{18}$ molecules m^{-2} is the surface density of BT molecules chemisorbed on a Au(111) surface.[56] The number of molecules in the confocal volume of the conventional Raman measurement is estimated with $N_{RS} = N_A(MW_{BT})^{-1}\rho_{BT}V_{CV} \approx 9.3 \times 10^9$ molecules, where N_A = 6.02×10^{23} molecules mol^{-1}, MW_{BT} =110.18 g mol^{-1} is the molecular weight, $\rho_{BT} \approx 1.08$ g cm^{-3} is the density, and $V_{CV} \approx 1.6 \times 10^{-18}$ m^3 is the experimentally determined confocal volume of the measurement system. The integrated intensity of the conventional Raman spectrum from a neat BT solution in a sealed glass vial is $\kappa_{NR}^{1094} \approx 76$ photons s^{-1}, which is measured with 2 mW laser power (λ_o = 632.8 nm) and 100 ms integration time. The mean spatially averaged integrated intensity of the SERS measurement is $\bar{\kappa}^{1068} \approx 3.5 \times 10^5$ photons s^{-1}, and therefore, the mean spatially averaged Raman enhancement is ${}^{AEF}\bar{G}^{1068} \approx 1.2 \times 10^7$.

Conflict of Interest: The authors declare no competing financial interest.

Acknowledgment. The authors thank Jan van Nieuwkasteele and Johan Bomer for helpful comments with device processing, Mark Smithers for assistance with SEM imaging, and Eddy de Weerd for assistance with AFM imaging. LLTN thanks the Vietnamese Overseas Scholarship Program (Project No. 322) for financial support. Partial financial support was received from the Innovative Medicines Initiative, a public−private partnership between the European Union and the European Federation of Pharmaceutical Industries and Associations (RAPP-ID, Project No. 115153).

Supporting Information Available: SEM images of Ag-NW arrays with λ_g = 200 nm, g = 20 nm, curve fitting results of the nanogap reduction parameter α, Au-NW array cross-section SEM images with λ_g = 100 nm, w = 50 nm, and t_z = 70 nm that were prepared with focused ion-beam milling, conventional Raman spectroscopy measurements of neat benzenethiol in a sealed glass vial, and SERS measurements of benzenethiol chemisorbed on Ag-NW arrays surfaces. This material is available free of charge *via* the Internet at http://pubs.acs.org.

REFERENCES AND NOTES

1. Xia, Y.; Yang, P.; Sun, Y.; Wu, Y.; Mayers, B.; Gates, B.; Yin, Y.; Kim, F.; Yan, H. One-Dimensional Nanostructures: Synthesis, Characterization, and Applications. *Adv. Mater.* **2003**, *15*, 353–389.
2. Agrait, N.; Yeyati, A. L.; van Ruitenbeek, J. M. Quantum Properties of Atomic-Sized Conductors. *Phys. Rep.* **2003**, *377*, 81–279.
3. Kast, K.; Schroeder, P.; Hyun, Y J.; Pongratz, P.; Bruückl, H. Synthesis of Single-Crystalline Zn Metal Nanowires Utilizing Cold-Wall Physical Vapor Deposition. *Nano Lett.* **2007**, *7*, 2540–2544.
4. Xiang, C.; Kung, S.-C.; Taggart, D. K.; Yang, F.; Thompson, M. A.; Güell, A. G.; Yang, Y.; Penner, R. M. Lithographically Patterned Nanowire Electrodeposition: A Method for Patterning Electrically Continuous Metal Nanowires on Dielectrics. *ACS Nano* **2008**, *2*, 1939–1949.
5. Kulkarni, G. U.; Radha, B. Metal Nanowire Grating Patterns. *Nanoscale* **2010**, *2*, 2035–2044.
6. Chen, X.; Guo, Z.; Yang, G.-M.; Li, J.; Li, M.-Q.; Liu, J.-H.; Huang, X. J. Electrical Nanogap Devices for Biosensing. *Mater. Today* **2010**, *13*, 28–41.
7. Maier, S. A.; Atwater, H. Plasmonics: Localization and Guiding of Electromagnetic Energy in Metal/Dielectric Structures. *J. Appl. Phys.* **2005**, *98*, 011101.
8. Müller, K. A. Ga^+-Ion Beams on Gold: Sputter Yields and Redeposition. *Microelectron. Eng.* **1990**, *11*, 443–447.
9. Raether, H. *Surface Plasmons on Smooth and Rough Surfaces and on Gratings*; Springer: Berlin, Germany, 1988.
10. Xuegong, D.; Braun, G. B.; Liu, S.; Sciortino, P. F., Jr.; Koefer, B.; Tombler, T.; Moskovits, M. Single-Order, Subwavelength Resonant Nanograting as a Uniformly Hot Substrate for Surface-Enhanced Raman Spectroscopy. *Nano Lett.* **2010**, *10*, 1780–1786.
11. Siegfried, T.; Ekinci, Y.; Solak, H. H.; Martin, O. J. F.; Sigg, H. Fabrication of Sub-10 nm Gap Arrays Over Large Areas for Plasmonic Sensors. *Appl. Phys. Lett.* **2011**, *99*, 263302.
12. Jin, M.; van Wolferen, H.; Wormeester, H.; van den Berg, A.; Carlen, E. T. Large-Area Nanogap Plasmon Resonator Arrays for Plasmonics Applications. *Nanoscale* **2012**, *4*, 4712–4718.
13. Singh, P. S.; Kätelhön, E.; Mathwig, K.; Wolfrum, B.; Lemay, S. Stochasticity in Single-Molecule Nanoelectrochemistry: Origins, Consequences, and Solutions. *ACS Nano* **2012**, *6*, 9662–9671.
14. Halas, N. J.; Lal, S.; Chang, W.-S.; Link, S.; Nordlander, P. Plasmons in Strongly Coupled Nanostructures. *Chem. Rev.* **2011**, *111*, 3913–3961.
15. Tour, J. M. Molecular Electronics. Synthesis and Testing of Components. *Acc. Chem. Res.* **2000**, *33*, 791–804.
16. Wu, D. Y.; Li, J. F.; Ren, B.; Tian, Z. Q. Electrochemical Surface-Enhanced Raman Spectroscopy of Nanostructures. *Chem. Soc. Rev.* **2008**, *37*, 1025–1041.
17. Matula, R. A. Electrical Resistivity of Copper, Gold, Palladium, and Silver. *J. Phys. Chem. Ref. Data* **1979**, *8*, 1147–1298.

18. Durkan, C.; Welland, M. E. Size Effects in the Electrical Resistivity of Polycrystalline Nanowires. *Phys. Rev. B* **2000**, *61*, 14215–14218.
19. Garcia-Vidal, F. J.; Pendry, J. B. Collective Theory for Surface Enhanced Raman Scattering. *Phys. Rev. Lett.* **1996**, *77*, 1163–1166.
20. Moskovits, M. Surface-Enhanced Spectroscopy. *Rev. Mod. Phys.* **1985**, *57*, 783–826.
21. Corrigan, T. D.; Guo, S.; Phaneuf, R. J.; Szmacinski, H. J. Enhanced Fluorescence from Periodic Arrays of Silver Nanoparticles. *Fluoresc.* **2005**, *15*, 777–784.
22. Stuart, S. R.; Hall, D. G. Absorption Enhancement in Silicon-on-Insulator Waveguides Using Metal Island Films. *Appl. Phys. Lett.* **1998**, *73*, 3815–3817.
23. Zia, R.; Schuller, J. A.; Chandran, A.; Brongersma, M. L. Plasmonics—The Wave of Chip-Scale Device Technologies. *Mater. Today* **2006**, *9*, 20–27.
24. Link, S.; ElSayed, M. A. Spectral Properties and Relaxation Dynamics of Surface Plasmon Electronic Oscillations in Gold and Silver Nanodots and Nanorods. *J. Phys. Chem. B* **1999**, *103*, 8410–8426.
25. Jackson, J. B.; Halas, N. J. Surface-Enhanced Raman Scattering on Tunable Plasmonic Nanoparticle Substrates. *Proc. Natl. Acad. Sci. U.S.A.* **2004**, *101*, 17930–17935.
26. Lu, Y.; Liu, G. L.; Kim, J.; Mejia, Y. X.; Lee, L. P. Nanophotonic Crescent Moon Structures with Sharp Edge for Ultrasensitive Biomolecular Detection by Local Electromagnetic Field Enhancement Effect. *Nano Lett.* **2005**, *5*, 119–124.
27. Rodríguez-Lorenzo, L.; ÁlvarezPuebla, R. A.; Pastoriza-Santos, I.; Mazzucco, S.; Stéphan, O.; Kociak, M.; Liz-Marzán, L. M.; García de Abajo, F. J. Zeptomol Detection through Controlled Ultrasensitive Surface-Enhanced Raman Scattering. *J. Am. Chem. Soc.* **2009**, *131*, 4616–4618.
28. Shanmukh, S.; Jones, L.; Driskell, J.; Zhao, Y.; Dluhy, R.; Tripp, R. A. Rapid and Sensitive Detection of Respiratory Virus Molecular Signatures Using a Silver Nanorod Array SERS Substrate. *Nano Lett.* **2006**, *6*, 2630–2636.
29. Hulteen, J. C.; Van Duyne, R. P. Nanosphere Lithography: A Materials General Fabrication Process for Periodic Particle Array Surfaces. *J. Vacuum Sci. Technol. A* **1995**, *13*, 1553–1558.
30. Kitson, S. C.; Barnes, W. L.; Sambles, J. R. Full Photonic Band Gap for Surface Modes in the Visible. *Phys. Rev. Lett.* **1996**, *77*, 2670–2673.
31. Gunnarsson, L.; Bjerneld, E. J.; Xu, H.; Petronis, S.; Kasemo, B.; Käll, M. Interparticle Coupling Effects in Nanofabricated Substrates for Surface-enhanced Raman Scattering. *Appl. Phys. Lett.* **2001**, *78*, 802–804.
32. Abu Hatab, N. A.; Oran, J. M.; Sepaniak, M. J. Surface-Enhanced Raman Spectroscopy Substrates Created *via* Electron Beam Lithography and Nanotransfer Printing. *ACS Nano* **2008**, *2*, 377–385.
33. Brolo, A. G.; Arctander, E.; Gordon, R.; Leathem, B.; Kavanagh, K. L. Nanohole-Enhanced Raman Scattering. *Nano Lett.* **2004**, *4*, 2015–2018.
34. Fromm, D. P.; Sundaramurthy, A.; Schuck, P. J.; Kino, G.; Moerner, W. E. Gap-Dependent Optical Coupling of Single "Bowtie" Nanoantennas Resonant in the Visible. *Nano Lett.* **2004**, *4*, 957–961.
35. Porto, J. A.; Garcia-Vidal, F. J.; Pendry, J. B. Transmission Resonances on Metallic Gratings with Very Narrow Slits. *Phys. Rev. Lett.* **1999**, *83*, 2845–2848.
36. Fleischmann, M.; Hendra, P. J.; McQuillan, A. J. Raman Spectra of Pyridine Adsorbed at a Silver Electrode. *Chem. Phys. Lett.* **1974**, *26*, 163–166.
37. Perney, N. M. B.; Baumberg, J. J.; Zoorob, M. E.; Charlton, M. D. B.; Mahnkopf, S.; Netti, C. M. Tuning Localized Plasmons in Nanostructured Substrates for Surface-Enhanced Raman Scattering. *Opt. Express* **2006**, *14*, 847–857.
38. Gao, H.; Henzie, J.; Lee, M. H.; Odom, T. W. Screening Plasmonic Materials using Pyramidal Gratings. *Proc. Natl. Acad. Sci. USA* **2008**, *105*, 20146–20151.
39. Lin, T.-H.; Linn, N. C.; Tarajano, L.; Jiang, B.; Jiang, P. Electrochemical SERS at Periodic Metallic Nanopyramid Arrays. *J. Phys. Chem. C* **2009**, *113*, 1367–1372.
40. Wu, H.-Y.; Choi, C. J.; Cunningham, B. T. Plasmonic Nanogap-Enhanced Raman Scattering Using a Resonant Nanodome Array. *Small* **2012**, *8*, 2878–2885.
41. Wood, R. W. On a Remarkable Case of Uneven Distribution of Light in a Diffraction Grating Spectrum. *Phil. Mag.* **1902**, *4*, 396–402.
42. Tsang, J. C.; Kirtley, J. R.; Bradley, J. A. Surface-Enhanced Raman Spectroscopy and Surface Plasmons. *Phys. Rev. Lett.* **1979**, *43*, 772–775.
43. Girlando, A.; Philpott, M. R.; Heitmann, D.; Swalen, J. D.; Santo, R. Raman Spectra of Thin Organic Films Enhanced by Plasmon Surface Polaritons on Holographic Metal Gratings. *J. Chem. Phys.* **1980**, *72*, 5187–5191.
44. Weber, M.; Mills, D. L. Interaction of Electromagnetic Waves with Periodic Gratings: Enhanced Fields and the Reflectivity. *Phys. Rev. B* **1983**, *27*, 2698–2709.
45. Baltog, I.; Primeau, N.; Reinisch, R. Surface Enhanced Raman Scattering on Silver Grating: Optimized Antenna-like Gain of the Stokes Signal of 10^4. *Appl. Phys. Lett.* **1995**, *66*, 1187–1189.
46. Sobnack, M. B.; Tan, W. C.; Wanstall, N. P.; Preist, T. W.; Sambles, J. R. Stationary Surface Plasmons on a Zero-Order Metal Grating. *Phys. Rev. Lett.* **1998**, *80*, 5667–5670.
47. Barnes, W. L.; Dereux, A.; Ebbesen, T. W. Surface Plasmon Subwavelength Optics. *Nature* **2003**, *424*, 824–830.
48. Jin, M.; Pully, V.; Otto, C.; van den Berg, A.; Carlen, E. T. High-Density Periodic Arrays of Self-Aligned Subwavelength Nanopyramids for Surface-Enhanced Raman Spectroscopy. *J. Phys. Chem. C* **2010**, *114*, 21953–21959.
49. Wang, F.; Shen, R. General Properties of Local Plasmons in Metal Nanostructures. *Phys. Rev. Lett.* **2006**, *97*, 206806.
50. Arnold, M. D.; Blaber, M. G. Optical Performance and Metallic Absorption in Nanoplasmonic Systems. *Opt. Express* **2009**, *17*, 3835–3847.
51. Born, M.; Wolf, E. *Principles of Optics*, 7th ed.; Cambridge University Press: Cambridge, MA, 1999.
52. Xu, H.; Aizpurua, J.; Käll, M.; Apell, P. Electromagnetic Contributions to Single-Molecule Sensitivity in Surface-Enhanced Raman Scattering. *Phys. Rev. E.* **2000**, *62*, 4318–4324.
53. Owen, T. *Fundamentals of Modern UV-Visible Spectroscopy: Primer*; Agilent Technologies: Santa Clara, CA, 2000; Pub. 5980-1397E.
54. Moerner, W. E. Examining Nanoenvironments in Solids on the Scale of a Single, Isolated Impurity Molecule. *Science* **1994**, *265*, 46–53.
55. Joo, T. H.; Kim, M. S.; Kim, K. Surface-Enhanced Raman Scattering of Benzenethiol in Silver Sol. *J. Raman Spectrosc.* **1987**, *18*, 57–60.
56. Wan, L.-J.; Terashima, M.; Noda, H.; Osawa, M. Molecular Orientation and Ordered Structure of Benzenethiol Adsorbed on Gold(111). *J. Phys. Chem. B* **2000**, *104*, 3563–3569.